Adaptive Nonlinear Active Disturbance Rejection Current Controller for Distributed Generation System Considering Uncertain Ripples

Zhenxing Cheng, Liyi Li, *Senior Member, IEEE*, Chengbao Zhong, Jinglong Wang, Xun Bai, and Jiaxi Liu

***Abstract*—The onboard distributed generation system with high-speed permanent magnet synchronous generator (PMSG) faces significant current ripples issue due to the low stator inductance. The complex operating conditions of the electric vehicles lead to uncertain periodic and nonperiodic disturbances in the current loop, which deteriorates the control performance of current loop. To address this issue, this article proposes an adaptive nonlinear active disturbance rejection current controller for the distributed generation system of onboard high-speed PMSG. The improved adaptive nonlinear controller offers disturbance rejection capabilities for different forms of nonperiodic disturbances avoiding complex cascade structure. Additionally, an adaptive internal model controller is embedded within the current controller to suppress periodic disturbances. Compared with the traditional method, this method improves the tracking ability of high-frequency periodic signals and shows strong robustness against dc offsets. The proposed method reduces current distortion by approximately 8% and decreases the frequency identification convergence time by about 40%. The stability of the closed-loop system is analyzed, and the controller parameters are tuned. Finally, the feasibility and effectiveness of the proposed current control strategy are validated on a 60 kW gas turbine-driven PMSG generation platform.**

***Index Terms*—Adaptive internal model control, high-speed permanent magnet synchronous generator (PMSG), nonlinear active disturbance rejection control (ADRC), onboard distributed generation system, uncertain current ripples.**

I. Introduction

RANGE-EXTENDED hybrid electric vehicles have demonstrated significant market potential as a transitional model. The current development trend for range-extended power systems focuses on modularization, high speed, and high-power density [1], [2]. High-speed permanent magnet synchronous generators (PMSGs) are widely used in electric vehicles due to their high reliability and high-power density. However, the design of small stator inductance in high-speed motors leads to severe current harmonics [3], [4]. Nonlinear factors such as mechanical imbalance, stator asymmetry, and electromagnetic interference from nonideal inverters exacerbate current harmonics [5]. Additionally, power electronic devices and load variations could induce current ripples. The current distortions caused by uncertain disturbances can be categorized into nonperiodic disturbances and periodic disturbances. These disturbances not only affect the quality of the output but also increase system losses and induce mechanical vibrations. Therefore, measures must be taken to mitigate the impact of current distortions in designing and operating current control loops for PMSGs. Common methods include enhancing mechanical manufacturing precision, optimizing stator winding design, improving magnet material and uniformity, and employing more accurate control algorithms [6], [7].

The proportional-integral (PI) controller is the most common method for current control, achieving precise current regulation by adjusting the proportional and integral coefficients. However, its effectiveness in suppressing high-frequency harmonics and nonlinear disturbances is limited, resulting in steady-state errors [8]. To enhance the performance of current controllers, various robust control theories have been introduced into the current loop, such as model predictive control, sliding mode control, and H∞ control [9], [10], [11]. Although the robust control method can improve the control performance of the nonlinear system, the stability of the system is still affected by uncertain disturbances.

To further enhance the disturbance rejection capability of the current loop, the extended state observer (ESO) has been introduced into the control loop. Numerous studies have focused on designing different types of observers to estimate disturbances in the current loop and use feedforward paths to compensate for disturbances in the output voltage command of the current controller [12], [13]. Among these methods, active disturbance rejection control (ADRC), closely integrated with ESOs, has been extensively researched and developed due to the strong robustness and real-time performance. ADRC improves the current loop with a robust capability to suppress impulsive nonperiodic disturbances [14]. However, ESOs are essentially low-pass filters and are ineffective against periodic disturbances

Received 14 August 2024; revised 28 October 2024; accepted 7 December 2024. Date of publication 11 December 2024; date of current version 28 January 2025. This work was supported in part by the National Key R&D Plan under Grant 2022YFB3402702 and in part by the Guangdong Provincial Key Laboratory under Grant 2020B121202017. Recommended for publication by Associate Editor R. Kennel. *(Corresponding author: Jiaxi Liu.)*

Zhenxing Cheng, Liyi Li, Jinglong Wang, Xun Bai, and Jiaxi Liu are with the Department of Electrical Engineering, Harbin Institute of Technology, Harbin 150001, China (e-mail: chengzhenxing@mail.sdu.edu.cn; liliyi@hit.edu.cn; 24b306005@stu.hit.edu.cn; 22s006038@stu.hit.edu.cn; liujiaxi@hit.edu.cn).

Chengbao Zhong is with the Equipment Power Technology Research Institute, Gree Electric Appliances, Zhuhai 510663, China (e-mail: gree_aem@cn.gree.com).

Color versions of one or more figures in this article are available at https://doi.org/10.1109/TPEL.2024.3515105.

Digital Object Identifier 10.1109/TPEL.2024.3515105

that exceed bandwidth [15]. For high-speed PMSGs, the fundamental frequency is much higher than that of servo motors. The 5th and 7th harmonics of the phase current exceed the bandwidth of ADRC. Consequently, the traditional ADRC cannot guarantee performance in high-speed motor applications.

In motor control systems requiring high-precision current and harmonic suppression, the multiple synchronous rotating reference frame (MSRF) method is widely applied [16], [17], [18]. This method uses multiple synchronous rotating coordinate transformations to convert current signals into dc quantities in the dq-axis synchronous rotating reference frame [19]. Low-pass filters are then used to extract harmonic signals at corresponding frequencies. The extracted harmonic components are used to calculate compensation signals, thereby suppressing harmonics at specific frequencies. However, the MSRF method needs multiple coordinate transformations and filtering processes, which increases the real-time computational burden of the system [20]. Low-pass filters can lead to phase delays, potentially affecting stability and dynamic response. This method is unsuitable for high-speed motors with high fundamental frequencies. Under rapidly changing operating conditions, this may result in a decrease in control accuracy.

To enhance the suppression capability of high-frequency periodic disturbances, various improved ADRC methods have been proposed. First, repetitive controllers have been integrated into ADRC, leveraging the repetitive nature of periodic signals to gradually reduce errors within each period, thereby suppressing periodic harmonics [21]. Similarly, resonant controllers, which excel in tracking sinusoidal signals, have been proposed to suppress specific periodic disturbances [6], [22]. However, these methods are complex in design and implementation and are sensitive to changes in system parameters. To address these issues, various improved resonant controllers have been proposed to improve robustness and stability [23], [24], [25]. For example, a quasi-resonant controller (QRC) has been integrated into the ADRC of the permanent magnet synchronous motor speed loop to achieve smooth speed regulation [25]. Compared to resonant controllers, QRCs offer faster response speeds and the capability to suppress multiple frequency harmonics [26]. However, these periodic disturbance suppression methods require the disturbance frequency to effectively suppress disturbances at specific frequencies. Zhu et al. [27] propose an adaptive switching high-order ESO-based enhanced speed controller for electric drives to suppress time-varying disturbances. The proposed speed controller achieves high disturbance estimation accuracy by increasing the asymptotic convergence speed of the higher-order terms. Although it does not require disturbance frequency information, it is only effective within a certain observable disturbance frequency range and is ineffective for rapidly changing disturbances [28].

To address this issue, Tian et al. [29], [30] propose an adaptive resonant controller (ARC) to identify the frequency of sinusoidal disturbance signals. This method significantly improves the ability to suppress unknown disturbances. However, the study points out that the proposed method has weak dynamic response capabilities and can only estimate periodic disturbances in steady-state conditions. The experimental motor in the study is still a low-speed motor, with identified current loop disturbance frequencies below 300 Hz. In high-speed motors with higher fundamental frequencies, the dynamic response capability of this method limits the disturbance suppression performance. Additionally, environmental factors, such as sensor dc bias and noise, affect the stability of the ARC. In summary, there is a gap in the methods for suppressing uncertain disturbances in the current loop in the field of high-speed motor applications.

This article proposes an improved adaptive nonlinear active disturbance rejection current controller for the distributed generation system of onboard high-speed PMSG. The main contributions of this article are summarized as follows.

1) An improved nonlinear function is introduced into the nonlinear ADRC (NADRC). This method avoids the cascade structure of the observer and the switching of weighting functions. While reducing control complexity, this method exhibits strong antidisturbance capability against nonperiodic disturbances.
2) An adaptive internal model controller (AIMC) is embedded into the NADRC system, achieving simultaneous suppression of both periodic and nonperiodic disturbances in the current loop. This method improves the identification speed of periodic disturbance frequencies, allowing for adaptive suppression of disturbances with uncertain frequencies. It also demonstrates strong antidisturbance capability against measurement noise.

This article is organized as follows. The gas turbine-driven PMSG distributed generation system is presented in Section II. The improved NADRC current loop controller is proposed in Section III. In Section IV, an AIMC is proposed to enhance robustness against periodic disturbances and dc bias. The effectiveness of the proposed control method is validated using a 60 kW gas turbine-driven PMSG experimental platform in Section V. Section VI provides a summary of the entire article.

II. Modeling of Current Loop NADRC

A. Mathematical Model

The fundamental voltage equations of PMSG in the dq reference frame, with current flowing out of the machine as the positive direction, are given as

$$\begin{cases} u_d = -R_s i_d - L_d \frac{di_d}{dt} + \omega_e L_q i_q \\ u_q = -R_s i_q - L_q \frac{di_q}{dt} + \omega_e \psi_f - \omega_e L_d i_d \end{cases} \tag{1}$$

where R_s is the stator resistance; L_d and L_q are the direct-axis inductance and quadrature-axis inductance, respectively. u_d and u_q are the d-axis and q-axis components of the stator voltage, respectively. $i_d$and i_q are the d-axis and q-axis components of the stator current, respectively. ω_e is the electrical angular speed. ψ_f is the permanent magnet flux linkage.

Due to factors such as three-phase imbalance and nonlinear magnetic circuits, the fifth and seventh harmonics of the phase current in PMSG are the most significant [5]. Taking phase-A as an example, the expressions for the fifth and seventh harmonic back electromotive force (EMF) are as follows:

$$e_a = -\omega_e \psi_1 \sin(\omega_e t) - 5\omega_e \psi_5 \sin(5\omega_e t + \theta_5)$$

$$-7\omega_e\psi_7\sin(7\omega_e t+\theta_7) \tag{2}$$

where θ represents the initial phase, and the subscripts indicate the variables corresponding to the harmonic order. The back EMF of phase-B and phase-C lag behind that of phase-A by 120° sequentially.

Transform (2) into the dq rotating coordinate system, the fifth and seventh harmonic back EMF exhibit sixth harmonic characteristics as

$$\begin{bmatrix}\psi_{fd}\\ \psi_{fq}\end{bmatrix}=\begin{bmatrix}\psi_1-\psi_5\cos(6\omega_e t+\theta_5)+\psi_7\cos(6\omega_e t+\theta_7)\\ \psi_5\sin(6\omega_e t+\theta_5)+\psi_7\sin(6\omega_e t+\theta_7)\end{bmatrix}. \tag{3}$$

Substituting (3) into (1) yields the PMSG model that considers the fifth and seventh harmonic back EMFs

$$\begin{cases}u_d=-R_s i_d-L_d\frac{di_d}{dt}+\omega_e L_q i_q\\ \qquad +5\omega_e\psi_5\sin(6\omega_e t+\theta_5)-7\omega_e\psi_7\sin(6\omega_e t+\theta_7)\\ u_q=-R_s i_q-L_q\frac{di_q}{dt}+\omega_e\psi_f-\omega_e L_d i_d\\ \qquad +5\omega_e\psi_5\cos(6\omega_e t+\theta_5)+7\omega_e\psi_7\cos(6\omega_e t+\theta_7)\end{cases}. \tag{4}$$

In addition to the fifth and seventh harmonics with determined frequencies, there are also nonfundamental frequency integer multiples of ripple caused by nonlinearity in the phase current. These disturbances are difficult to model quantitatively. Utilizing the concept of ADRC, both known and unknown disturbances in the current loop are treated as total disturbance. Thus, (1) can be rewritten as

$$\begin{cases}\frac{di_d}{dt}=b_0u_d+f_{dt}\\ \frac{di_q}{dt}=b_0u_q+f_{qt}\end{cases}. \tag{5}$$

Here, f_{dt} and f_{qt} represent the total disturbances in the d-axis and q-axis, respectively. b_0 is the known gain. For surface-mounted PMSG, $L_d=L_q$ and $b_0=-1/L_d$.

B. Traditional Current ADRC

For the current loop of surface-mounted PMSG, the $i_d=0$ control strategy is adopted. The design of current controller uses the q-axis as an example. First, based on the principle of ADRC, a linear ESO is established to observe the feedback current and total disturbance

$$\begin{cases}e_L=i_q-z_{11}\\ \dot{z}_{11}=b_0u_q+z_{12}+\beta_1e_L\\ \dot{z}_{12}=\beta_2e_L\end{cases} \tag{6}$$

where z_{11} is the estimated value of the q-axis current, and z_{12} is the observed value of the total disturbance on the q-axis. e_L represents the current error. β_1 and β_2 are the observer gains.

The state error feedback (SEF) design for linear ADRC (LADRC) is

$$u_q^*=(K_pe_L-z_{12})/b_0 \tag{7}$$

where K_p represents the proportional gain of the controller.

To enhance the flexibility of LADRC parameters, a nonlinear function is introduced into ADRC. The nonlinear ESO (NESO) of (5) is implemented as

$$\begin{cases}e_N=i_q-z_{21}\\ \dot{z}_{21}=b_0u_q+z_{22}+\beta_3fal(e_N,\alpha_1,\delta_1)\\ \dot{z}_{22}=\beta_4fal(e_N,\alpha_2,\delta_2)\end{cases} \tag{8}$$

where z_{21} and z_{22} are the estimated feedback current and total disturbance by the NESO. β_3 and β_4 represent the NESO gains. $fal()$ is the nonlinear function [31]. α_1, α_2, δ_1, and δ_2 are the nonlinear parameters.

The SEF design for NADRC is

$$u_q^*=(\beta_5fal(e_N,\alpha_3,\delta_3)-z_{22})/b_0. \tag{9}$$

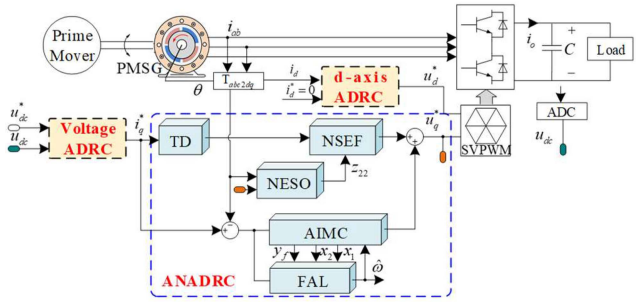

Fig. 1. Block diagram for the gas turbine-driven PMSG system with ANADRC current control.

III. Adaptive NADRC Current Control

The proposed adaptive NADRC current control block diagram for the gas turbine-driven PMSG system is shown in Fig. 1. The power generation system adopts a dual-loop control structure with both voltage and current loops, where the outer voltage loop uses a NADRC controller. The diagram shows the structure of the q-axis current adaptive NADRC (ANADRC) controller, which is identical to the d-axis current controller. The proposed ANADRC consists of two parts: the first part includes a tracking differentiator, an improved NESO, and a nonlinear SEF (NSEF) to suppress nonperiodic disturbances in the current loop. The second part comprises an AIMC and a frequency adaptive law (FAL) to suppress periodic disturbances in the current loop. The detailed specifics of the controller are introduced as follows.

A. Improved NADRC

As demonstrated in Section II, both LADRC and NADRC have respective advantages. LADRC exhibits stronger disturbance rejection capabilities against large disturbances, whereas the more flexible NADRC shows smaller steady-state errors for small disturbances but lacks rapid response to large disturbances. Previous studies have integrated the strengths of both approaches using weighted functions or cascaded forms, which results in overly complex controllers [32]. This section optimizes traditional ADRC by improving the nonlinear function and expanding the gain in the nonlinear region.

The structure of the proposed improved ANADRC for the PMSG power generation system is shown in Fig. 2. First, the NESO is established using an improved nonlinear function

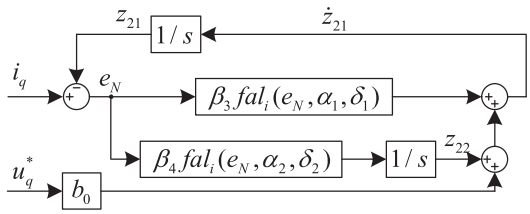

Fig. 2. Block diagram of the improved NESO structure.

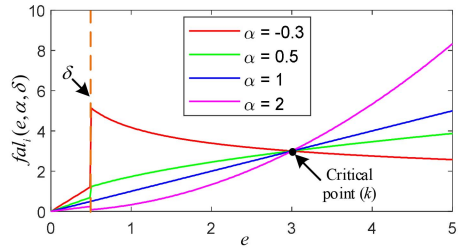

Fig. 3. Function characteristic curve of $fal_i(e,\alpha,\delta)$.

$fal_i(e,\alpha,\delta)$ to estimate the feedback bus voltage and total disturbances.

The improved nonlinear function $fal_i(e,\alpha,\delta)$ is defined as

$$fal_i(e,\alpha,\delta)=\begin{cases}k|e/k|^{\alpha}\text{sign}(e/k) & ,|e|>\delta\\ e/\delta^{1-\alpha} & ,|e|\le\delta\end{cases} \tag{10}$$

where k is the nonlinear weighting parameter.

By substituting (10) into (8), the current loop NADRC can be rewritten as

$$\begin{cases}e_N=i_q-z_{21}\\ \dot{z}_{21}=b_0u_q+z_{22}+\beta_3 fal_i(e_N,\alpha_1,\delta_1)\\ \dot{z}_{22}=\beta_4 fal_i(e_N,\alpha_2,\delta_2)\end{cases}. \tag{11}$$

The gain curve of the $fal_i(e,\alpha,\delta)$ nonlinear function under different values of α is shown in Fig. 3. For the PMSG current loop, the desired controller gain should be such that it is not too large for large errors to reduce surge currents. Conversely, for small errors, the gain should be increased to enhance tracking performance and reduce steady-state errors. As shown in Fig. 3, when $0<\alpha<1$, the gain characteristics meet these desired properties. Typically, α is set to 0.5 to balance nonlinear and linear gains.

To facilitate the characterization of the nonlinear function for different errors, the equivalent gain theory is employed and processed as follows:

$$\tau(e)=\frac{fal_i(e,\alpha,\delta)}{e}. \tag{12}$$

$\tau(e)$ can be equivalently represented as a variable gain function. As shown in Fig. 4(a), the bandwidth gain δ affects the width of the linear region of the nonlinear function. Based on existing literature works, δ is generally chosen such that $0.02<\delta<0.1$. The nonlinear factor α influences the degree of nonlinearity of the function. The $fal_i(e,\alpha,\delta)$ ensures a larger gain when the error is small. However, an excessively large value of α

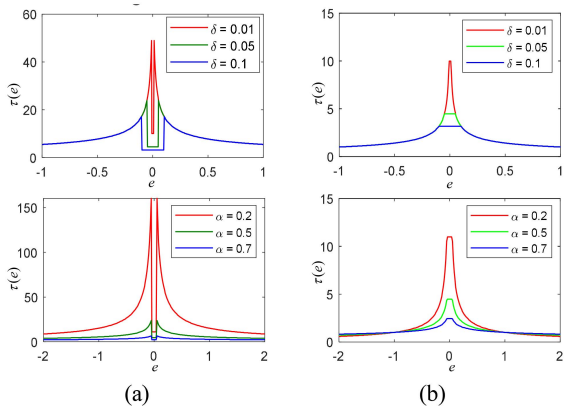

Fig. 4. Comparison of $\tau(e)$with different δ and α. (a) Proposed $fal_i(e,\alpha,\delta)$. (b) Traditional $fal(e,\alpha,\delta)$ [32].

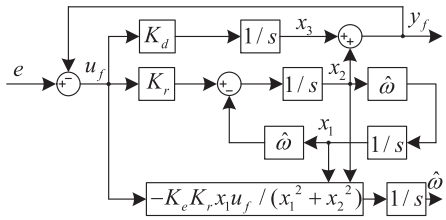

Fig. 5. Block diagram of the proposed AIMC.

may cause oscillations in the control loop. Compared with the traditional nonlinear function shown in Fig. 4(b), the improved nonlinear function increases the gain at the region switching points and for large errors while maintaining the same linear region. This enhancement improves the response speed of the controller to large errors.

B. Design of AIMC and FAL

When addressing harmonic disturbances beyond a certain frequency, ADRC performs poorly. Professor Zhigang Gao pointed out that when tuning ADRC parameters, ADRC essentially acts as a low-pass filter with a certain bandwidth. To address these issues, this article proposes an improved AIMC, as shown in Fig. 5.

Compared to traditional ARC [29], the proposed AIMC adds two additional loops. The output y_f feedback loop ensures the stability of disturbance frequency identification during dynamic processes. The state variable x_3 loop is used to eliminate the influence of dc bias in the input signal, preventing identification failures caused by nonsinusoidal signals.

The implementation of the observer for the system, considering the AIMC, is as follows:

$$\begin{cases}e_N=i_q-z_{21}\\ \dot{z}_{21}=b_0u_q+z_{22}+\beta_3 fal_i(e_N,\alpha_1,\delta_1)+x_2\\ \dot{z}_{22}=\beta_4 fal_i(e_N,\alpha_2,\delta_2)\\ \dot{x}_1=\hat{\omega}x_2\\ \dot{x}_2=-\hat{\omega}x_1-K_rx_2-K_rx_3+K_re_f\\ \dot{x}_3=-K_dx_2-K_dx_3+K_de_f\end{cases} \tag{13}$$

where K_r and K_d are constant gains. $\hat{\omega}$ is the estimated disturbance frequency. e_f represents the output error of the AIMC and $e_f = i_q^* - i_q$.

Based on the transfer function block diagram shown in Fig. 5, the transfer functions of the AIMC output y_f with respect to the input u_f, and the variable u_f with respect to the voltage error e, are derived as follows:

$$\begin{cases} G_{u_f,y_f} = \frac{s^2(K_d+K_r)+K_d\hat{\omega}^2}{s(s^2+\hat{\omega}^2)} \\ G_{u_f,e} = \frac{(s^2+\hat{\omega}^2)s}{H(s)} \end{cases} \tag{14}$$

where $H(s) = s^3 + (K_r + K_d)s^2 + \hat{\omega}^2 s + \hat{\omega}^2 K_d$.

By substituting the transfer function relationships of each variable with respect to the input u_f into (14), the following expression is obtained:

$$\begin{cases} G_{x_1,e} = K_r s\hat{\omega}/H(s) \\ G_{x_2,e} = K_r s^2/H(s) \\ G_{x_3,e} = K_d(s^2+\hat{\omega}^2)/H(s) \end{cases}. \tag{15}$$

Let the current error caused by the periodic disturbance signal in the current loop be represented as $e = a\sin(\omega t + \varphi) + D$.

By substituting $e = a\sin(\omega t + \varphi) + D$ into (15) and performing the inverse Laplace transform, the expressions for each state variable can be obtained as

$$\begin{cases} x_1(t) = \hat{\omega}E\sin(\omega t + \varphi + \phi) \\ x_2(t) = \omega E\cos(\omega t + \varphi + \phi) \\ x_3(t) = aK_d\left|1/H(j\omega)\right|(\hat{\omega}^2 - \omega^2)\sin((\omega t + \varphi) \\ \qquad +\angle(1/H(j\omega))) + D \end{cases} \tag{16}$$

where $E = aK_r|F(j\omega)|$, $\phi = \angle(F(j\omega))$, $F = s/H(s)$.

The expression for the angle can be obtained by performing an arctangent operation on the variables x_1 and x_2, as

$$\tan^{-1}\left(\frac{\omega x_1(t)}{\hat{\omega}x_2(t)}\right) = \omega t + \varphi + \phi. \tag{17}$$

By differentiating (17), the expression for the angular frequency ω can be obtained as

$$\frac{d}{dt}\left(\tan^{-1}\left(\frac{\omega x_1(t)}{\hat{\omega}x_2(t)}\right)\right) = \omega. \tag{18}$$

Based on (18), the estimation error for the disturbance frequency $\tilde{\omega}$ can be expressed as

$$\tilde{\omega} = \hat{\omega} - \frac{\hat{\omega}\omega(\dot{x}_1x_2 - x_1\dot{x}_2)}{(\omega x_1)^2 + (\hat{\omega}x_2)^2}. \tag{19}$$

By utilizing an integral controller to make the frequency estimation error shown in (19) equal to zero, the following condition can be obtained:

$$\dot{\hat{\omega}} = -K_e\tilde{\omega} = -K_e\left(\hat{\omega} - \frac{\hat{\omega}\omega(\dot{x}_1x_2 - x_1\dot{x}_2)}{(\omega x_1)^2 + (\hat{\omega}x_2)^2}\right). \tag{20}$$

As the frequency estimate iteratively converges to the actual value, substituting ω with $\hat{\omega}$ in (20) yields

$$\hat{\omega} = \hat{\omega}_0 - K_e\int_{t_0}^{t}\frac{K_r x_1(e - x_2 - x_3)}{{x_1}^2 + {x_2}^2}. \tag{21}$$

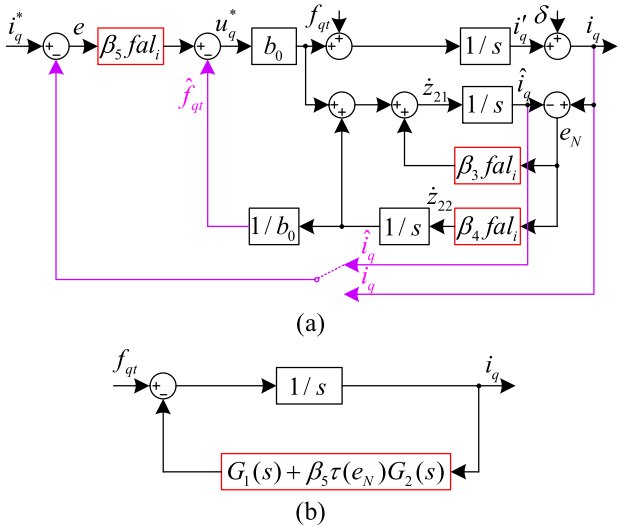

Fig. 6. System block diagram. (a) Proposed NADRC system for current control. (b) Equivalent negative feedback system.

In the digital implementation of the algorithm, this article utilizes the rectangular integration method to discretize the control approach. The discretization expression for the disturbance frequency is

$$\hat{\omega}(t) = \hat{\omega}(t-1) - \frac{K_eK_rx_1(t)(e(t) - x_2(t) - x_3(t))}{{x_1(t)}^2 + {x_2(t)}^2}T_s \tag{22}$$

where T_s is the sampling frequency.

The stability of the algorithm is discussed in detail in the Section IV. Based on the above calculations, the total disturbance estimate for the current loop is obtained as

$$\hat{f}_{qt} = z_{22} + x_2. \tag{23}$$

The NSEF for the adaptive ADRC can be designed as

$$i_q^* = \left(\beta_5 fal_i\left(e_N, \alpha_3, \delta_3\right) - z_{22} - x_2\right)/b_0. \tag{24}$$

IV. System Stability Analysis

A. Stability Analysis of the Improved NADRC

This section analyzes the disturbance rejection stability of the proposed NADRC method through transfer functions. Based on (5), (11), and (24), the block diagram of the current loop is shown in Fig. 6(a). From Fig. 6(a), the nonlinear component represented in the red block diagram is characterized by (12). The transfer functions of the proposed NESO disturbance estimation and the q-axis current estimation with respect to the system output are, respectively, as follows:

$$G_1(s) = \frac{F_{qt}(s)}{I_q(s)} = \frac{\beta_4\tau(e_N)(s + \beta_5\tau(e_N))}{s(s + \beta_5\tau(e_N) + \beta_3\tau(e_N))} \tag{25}$$

$$G_2(s) = \frac{\hat{I}_q(s)}{I_q(s)} = \frac{\beta_3\tau(e_N)}{s + \beta_5\tau(e_N) + \beta_3\tau(e_N)}. \tag{26}$$

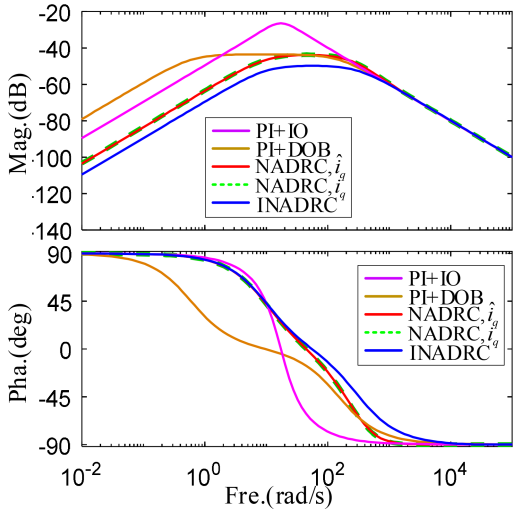

Fig. 7. Bode diagram of the transfer function $G_d(s)$.

From (25) and (26), the equivalent negative feedback model of the system can be represented as shown in Fig. 6(b). The disturbance transfer function of the current loop can be expressed as

$$G_d(s) = \frac{I_q(s)}{F_{qt}(s)} = \frac{s(s+\beta_3\tau(e_N)+\beta_5\tau(e_N))}{(s+\beta_5\tau(e_N))(s^2+s\beta_3\tau(e_N)+\beta_5\tau(e_N))}. \quad (27)$$

Fig. 7 compares the Bode plots of the disturbance transfer functions for different current controllers [33]. As shown in the figure, the NADRC controller exhibits stronger disturbance rejection capabilities compared to the traditional linear PI controller, which uses an integral observer and disturbance observer (DOB). The disturbance rejection performance of the NADRC current loop, whether using the actual or estimated q-axis current feedback, is comparable. The proposed improved NADRC controller achieves the smallest q-axis current response magnitude caused by disturbances, providing optimal disturbance rejection performance. However, it should be noted that the NADRC exhibits stronger attenuation of low- and high-frequency disturbances but weaker attenuation in the mid-frequency range.

According to Fig. 6, the transfer function of the current loop output in response to measurement noise δ can be derived as follows:

$$G_n(s) = \frac{I_q(s)}{\delta(s)} = \frac{s(\beta_3\tau(e_N)+\beta_4\tau(e_N))+\beta_4\tau(e_N)\beta_5\tau(e_N)}{(s+\beta_5\tau(e_N))(s^2+s\beta_3\tau(e_N)+\beta_5\tau(e_N))}. \quad (28)$$

Fig. 8 shows the amplitude-frequency characteristics of noise suppression for different current loop controllers. As depicted, all controllers exhibit similar, relatively weak noise suppression in the low-frequency range. This indicates that the current loop has poor robustness to dc bias errors. In the mid-to-high frequency range, the proposed NADRC and the traditional

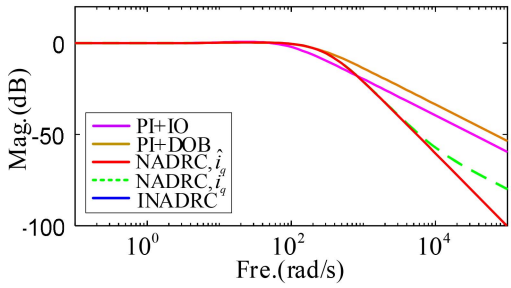

Fig. 8. Bode diagram of the transfer function $G_n(s)$.

NADRC, which uses estimated current feedback, demonstrate superior disturbance rejection compared to the other controllers.

In the mid-frequency range, the steady-state tracking error caused by disturbances in an ADRC system based on ESO is proportional to the rate of change of the disturbance. This is similar to most controllers, including PI controllers and controllers based on DOB. As a result, periodic disturbances may lead to a constant steady-state tracking error, which is unacceptable in many precision motor applications. To improve the suppression of periodic disturbances and dc bias errors, the stability of an improved NADRC with adaptive NESO is analyzed in Section IV-B.

B. Stability Analysis of the Adaptive NESO

The adaptive NESO shown in (13) consists of two parts: the improved NESO for estimating nonperiodic disturbances and the AIMC for estimating periodic disturbances. To facilitate the calculation, the periodic disturbance $f_p = a\cos(\omega_d t+\varphi)+D_{bias}$ is substituted into (13) and (20), and the stable solutions for each variable are obtained as $[i_q \quad d_{ap} \quad a\sin(\omega_d t+\varphi) \quad \ldots \quad a\cos(\omega_d t+\varphi) \quad \omega_3(0) \quad \omega_d]$.

By shifting the stable solutions of each variable to the origin of the state space, we obtain the following expressions for the transformed variables:

$$\begin{cases} \hat{i}_q = \hat{i}_{qe} + i_q \\ \hat{z}_{22} = \hat{z}_{22e} + f_{q\_ap} \\ \hat{x}_1 = \hat{x}_{1e} + a\sin(\omega_d t+\varphi) \\ \hat{x}_2 = \hat{x}_{2e} + a\cos(\omega_d t+\varphi) \\ \hat{x}_3 = \hat{x}_{3e} + \omega_3(0) \\ \hat{\omega}_d = \hat{\omega}_e + \omega_d \end{cases}. \quad (29)$$

Substituting (29) into (13) and simplifying, the resulting expression is

$$\dot{x}_e = A_e x_e + B_e = g(t, x_e, \hat{\omega}_e, K_{eq}) \quad (30)$$

where $x_e = [\ \hat{i}_{qe} \quad \hat{z}_{22e} \quad \hat{x}_{1e} \quad \hat{x}_{2e} \quad \hat{x}_{3e}\ ]^T$, $B_e = [0 \quad 0 \quad 0 \ \ldots -K_r\cos(\omega_d t+\varphi) - K_r D_{bias} - K_d\cos(\omega_d t+\varphi) - K_d D_{bias}]^T$

$$A_e = \begin{bmatrix} -\beta_3\tau & 1 & 0 & 1 & 0 \\ -\beta_4\tau & 0 & 0 & 0 & 0 \\ 0 & 0 & 0 & \omega_d & 0 \\ -K_r & 0 & -\omega_d & -K_r & -K_r \\ -K_d & 0 & 0 & -K_d & -K_d \end{bmatrix}.$$

Substituting (29) into (20), it can obtain

$$\frac{d}{dt}\hat{\omega}_e = K_{eq}\frac{\zeta_1(t)}{\zeta_2(t)} = f\left(t, x_e, \hat{\omega}_e, K_{eq}\right) \tag{31}$$

where $\zeta_1(t) = K_{eq}K_r(x_{1e} + a\sin(\omega_d t + \varphi))(u_{dce} + x_{2e} + a\cdot\cos(\omega_d t + \varphi) + x_{3e} + \omega_3(0))$, $\zeta_2(t) = {x_{1e}}^2 + {x_{2e}}^2 + a^2 + 2a\sqrt{2}\sin(\omega_d t + \varphi + \pi/4)$.

Let $K_{eq} = \varepsilon$, $\upsilon = \varepsilon t$, and ε represents a minimal value. Equations (30) and (31) can be rewritten as

$$\begin{cases} \varepsilon\frac{d}{d\upsilon}x_e = g(t, x_e, \hat{\omega}_e, \varepsilon) \\ \frac{d}{d\upsilon}\hat{\omega}_e = f(t, x_e, \hat{\omega}_e, \varepsilon) \end{cases}. \tag{32}$$

Equation (32) represents a typical form of a singular perturbation system. The stability proof of the singular perturbation system is provided by the following theorem [30].

Theorem 1: For the controlled plant $G(s)$, the necessary and sufficient condition for the existence of an ADRC controller $K(s)$ that ensures internal stability of the closed-loop system is that, when the periodic disturbance is nonzero, there exists a set of vectors $[\beta_3 \quad \beta_4 \quad K_r \quad K_d]$ such that the matrix A_e is positive definite and eigenvalues lie in the left half of the complex plane.

There exists a threshold ε^* such that for any ε within the range $0 < \varepsilon < \varepsilon^*$, the origin of the system in (32) is guaranteed to be exponentially stable.

Based on (30)–(32), the following observations can be made.

1) It holds that

$$\begin{cases} f(t, 0, 0, \varepsilon) = 0 \\ g(t, 0, 0, \varepsilon) = 0 \end{cases}. \tag{33}$$

2) The equation $0 = g(t, x_e, \hat{\omega}_e, 0)$ has a unique isolated solution given by $x_e = h(t, \hat{\omega}_e) = -A_e^{-1}B_e$, satisfying $h(t, 0) = 0$.
3) The functions f, g, h, along with their partial derivatives up to the second order, are bounded when $x_e - h(t, \hat{\omega}_e) \in B_\rho$, where B_ρ denotes a neighborhood surrounding $h(t, \hat{\omega}_e)$.
4) The origin of the boundary-layer system is described by

$$\frac{d}{d\tau}y = g\left(t, y + h\left(t, \hat{\omega}_e\right), \hat{\omega}_e, 0\right) \tag{34}$$

exhibits exponential stability uniformly with respect to $(t, \hat{\omega}_e)$.

Utilizing the stability criterion for singularly perturbed systems as outlined in [34], the theorem is validated once exponential stability of the origin for the reduced system (35) is established

$$\frac{d}{d\upsilon}\hat{\omega}_e = f(t, h(t, \hat{\omega}_e), \hat{\omega}_e, 0). \tag{35}$$

Substituting (16) and (29) into (20), (35) can be derived as

$$\frac{d}{dt}\hat{\omega}_e = -\varepsilon\frac{\hat{\omega}_e^2 - {\omega_d}^2}{\hat{\omega}_e}\frac{\sin^2\kappa}{\sin^2\kappa + \frac{{\omega_d}^2}{\hat{\omega}_e^2}\cos^2\kappa} \tag{36}$$

where $\kappa = \omega_d t + \varphi + \phi$.

The above equation represents the typical form of an averaged system theory. Within the sampling period T, the average value of (36) is

$$\bar{\hat{\omega}}_e = -\frac{\varepsilon}{\pi}\frac{\hat{\omega}_e^2 + 2\hat{\omega}_e\omega_d}{\hat{\omega}_e + \omega_d}\int_0^\pi \frac{\sin^2\kappa}{\sin^2\kappa + \frac{{\omega_d}^2}{(\hat{\omega}_e + \omega_d)^2}\cos^2\kappa}d\kappa$$
$$= -\varepsilon\hat{\omega}_e. \tag{37}$$

Combining (36) and (37) yields

$$\frac{d}{dt}\hat{\omega}_e = -\varepsilon\hat{\omega}_e. \tag{38}$$

Equation (38) indicates that the averaged system converges exponentially to the equilibrium point $(0, 0)$. This implies that the reduced system (34) is exponentially stable. Therefore, according to Theorem 1, the ANADRC closed-loop system represented by (32) is asymptotically stable.

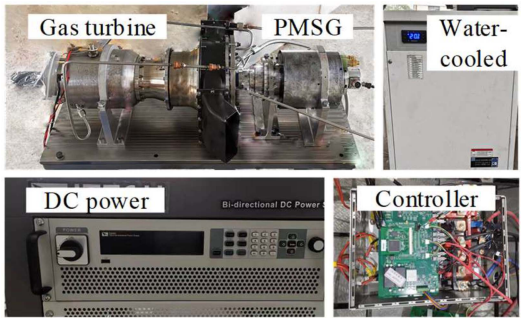

Fig. 9. Photograph of the PMSG experiment platform.

TABLE I
PARAMETERS OF THE EXPERIMENTAL PLATFORM

Parameter	Symbol	Value
Stator resistance	R_s	0.08 Ω
Stator inductance	L_s	0.052 mH
Pole pairs	p	1
Flux of the PM	Ψ_f	0.0278 Wb
Rated speed	n_N	60k r/min
Rated current	I_N	170 A
Rated power	P	60 kW

V. EXPERIMENTAL VALIDATION

An experimental setup for a turbine-driven 60-kW PMSG power generation system has been developed to verify the proposed methodology, as illustrated in Fig. 9. The system employs a surface-mounted PMSG powered by a gas turbine, with its parameters detailed in Table I. The turbine is regulated by a commercial drive unit. To emulate various operational scenarios, a bidirectional programmable dc power supply serves as the load. The control algorithm is executed using an STM32 + field programmable gate array (FPGA) architecture. The STM32F7X processor handles the control logic, and the XC6LX16 FPGA manages the external ADC and pulse width modulation signal generation. Both the switching and sampling frequencies are set at 20 kHz. The ADRC parameters are tuned based on the equivalent bandwidth theory. For the high-speed PMSG, with a rated frequency of 1000 Hz, the current loop bandwidth is set to 1200 Hz, and the observer bandwidth is set to 6000 Hz. The gain

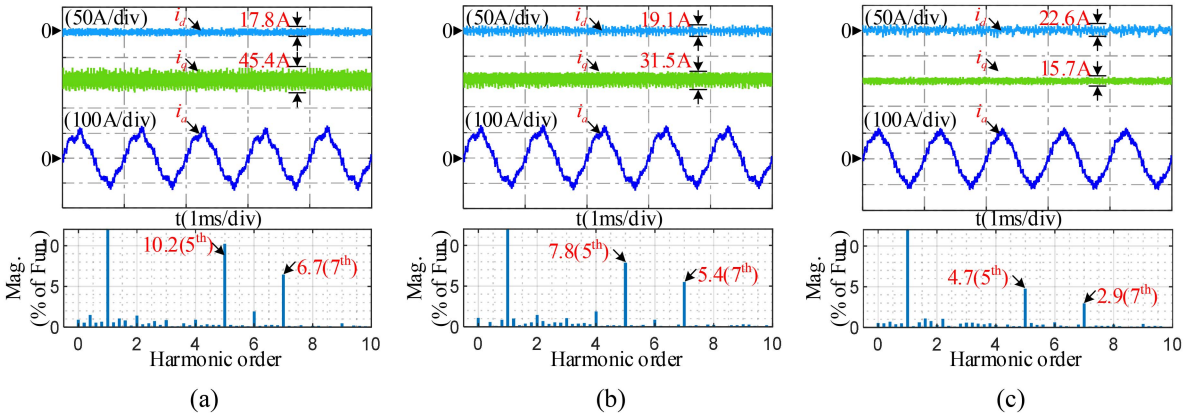

Fig. 10. Steady-state experiment results of traditional methods with 50% rated load power. (a) PI controller. (b) LADRC. (c) NADRC.

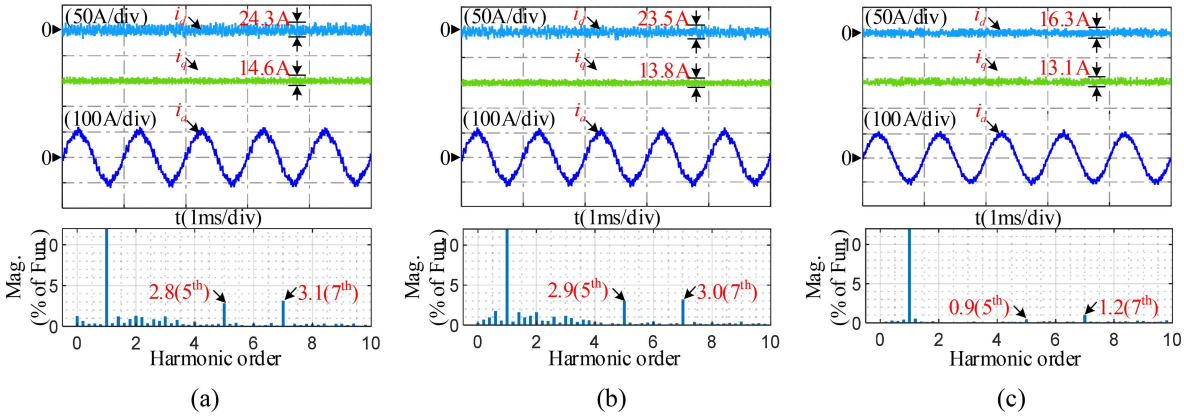

Fig. 11. Steady-state experiment results of enhanced methods with 50% rated load power. (a) SADRC. (b) HADRC. (c) Proposed ANADRC.

parameters of ADRC controllers are $\beta_1 = \beta_3 = 75360$, $\beta_2 = \beta_4 = 1.4 \times 10^9$, $K_p = 0.5$, $b_0 = 19230$. The parameters of the nonlinear function are selected as $\alpha_1 = \alpha_3 = 0.75$, $\alpha_2 = 0.5$, $\delta_i = 0.05$. The AIMC parameters are $K_r = 2000$, $K_e = 3$, and $K_d = 20$.

A. Steady-State Performance Experiment

Figs. 10 and 11 present comparison of steady-state experiment results with different methods at 50% rated load power. In the case of the PI controller, Fig. 10(a) shows that the q-axis current exhibits an unacceptable ripple. The phase-A current is severely distorted, with a total harmonic distortion (THD) of 16.9%. Fourier analysis of the phase current indicates that the 5th and 7th harmonics are significant. Fig. 10(b) and (c) compare the results of the traditional LADRC and NADRC. It can be observed that the current ripple is partially suppressed. The NADRC, which has smaller steady-state error characteristics, shows lower current harmonic content in the steady state. However, due to bandwidth limitations of the ESO, the 5th and 7th harmonics cannot be effectively suppressed.

Fig. 11 presents a comparison of experimental results for the improved ADRC controller. In Fig. 11(a), the switching ADRC (SADRC) proposed in [35] is used, where the linear/nonlinear controllers are switched based on the input error. The current waveform shows that the SADRC exhibits nonlinear controller characteristics in the steady state, with q-axis current ripple suppressed. However, due to frequent controller switching and the impact of delays, the d-axis current ripple increases. Fig. 11(b) shows the experimental results of the hybrid ADRC (HADRC), which uses a cascaded structure and weighting functions to avoid controller switching. Current analysis indicates that this method further reduces the current THD. However, due to the inclusion of LADRC characteristics in the weighting function, low-order current ripple slightly increases. Fig. 11(c) shows the experimental results of the proposed ANADRC controller. By improving the nonlinear function and integrating the advantages of NADRC, this method effectively suppresses the current ripple. Since there is no LADRC weighting or switching involved, the low-order ripple content does not increase. Additionally, under the action of AIMC, the 5th and 7th harmonics of the phase current are effectively suppressed. The current analysis results are shown in Table II, which demonstrates that the

TABLE II
COMPARISON OF STEADY-STATE CURRENT THD

Controller	THD	5th harmonic	7th harmonic	q-axis ripple
PI	16.9%	10.2%	6.7%	45.4 A
LADRC	15.2%	7.8%	5.4%	31.5 A
NADRC	12.6%	4.7%	2.9%	15.7 A
Switching ADRC	12.5%	2.8%	3.1%	14.6 A
Hybrid ADRC	12.4%	2.9%	3.0%	13.8 A
Proposed ANADRC	8.6%	0.9%	1.2%	13.1 A

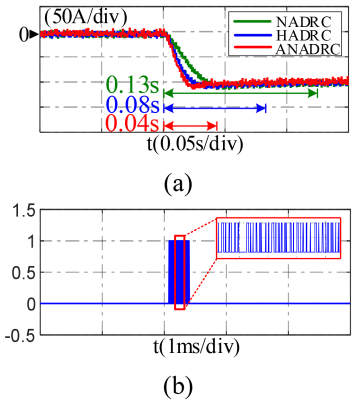

Fig. 12. Step experiment results of nonlinear current controllers. (a) Q-axis current. (b) Switching time of SADRC.

proposed ANADRC effectively suppresses uncertain current ripples.

B. Dynamic Performance Experiment

This section first compares the dynamic performance of ADRC current controllers with small current ripple through experiments. Fig. 12(a) shows the q-axis current curve when the system experiences a 50% sudden increase in rated load. Since the dynamic performance of SADRC and HADRC is consistent, only the HADRC current curve is presented. From the current curves, it can be seen that the traditional NADRC has weak tracking ability under large errors. In contrast, the improved HADRC, which integrates the advantages of both linear and nonlinear controllers, achieves fast performance similar to a linear controller while maintaining a small steady-state error. The q-axis current curve of the proposed ANADRC shows that it has a larger nonlinear gain under the same error, providing the best fast performance.

Fig. 12(b) presents the switching moments of the SADRC controller, where the high level indicates operation in the LADRC phase, and the low level indicates operation in the NADRC phase. To avoid frequent switching, the switching error is set to 20 A. It can be observed that during dynamic transitions, the SADRC undergoes repeated switching, causing frequent abrupt changes in the output of the current controller. The execution time of each program module on the control board was measured, and the results are shown in Table III. The

TABLE III
COMPARISON OF DYNAMIC PERFORMANCE

Controller	Stabilization time	Execution time
NADRC	0.13 s	12μs
SADRC	0.08 s	11μs
HADRC	0.08 s	16μs
ANADRC	0.04 s	13μs

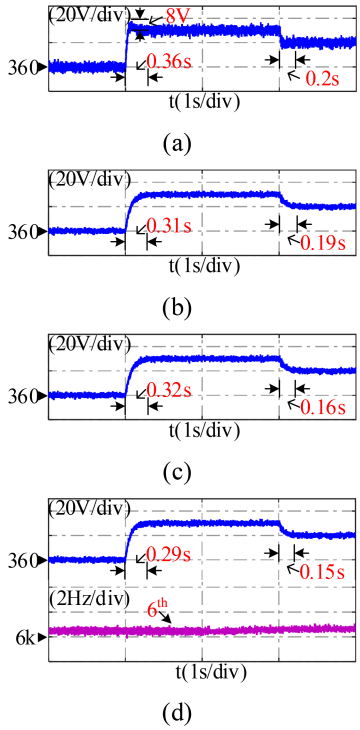

Fig. 13. Comparison of experiment results with voltage change under 20% rated load power. (a) PI controller. (b) LADRC. (c) NADRC. (d) Proposed ANADRC.

ANADRC has lower complexity compared to the HADRC with similar performance, resulting in a moderate computational load, which meets the requirements of the experimental platform.

Fig. 13 shows the experimental results comparing the dynamic performance of different controllers. Since the current loop adjusts very quickly and is minimally affected by external disturbances, this section compares the performance of the proposed improved NADRC with bus voltage as the benchmark. The PI controller causes significant dc bus voltage fluctuations due to severe current ripple, and there is an overshoot issue in the dc bus voltage when the voltage reference changes, as shown in Fig. 13(a). Comparing Fig. 13(b) and (c), the ADRC control method resolves the conflict between rapid response and overshoot. LADRC demonstrates better tracking capability than NADRC under large voltage reference changes, while the opposite is true for small voltage reference changes. NADRC exhibits smaller voltage fluctuations than LADRC due to its superior regulation ability for small errors. As shown in Fig. 13(c), the proposed improved NADRC offers optimal regulation capability for both large and small disturbances. The frequency estimate

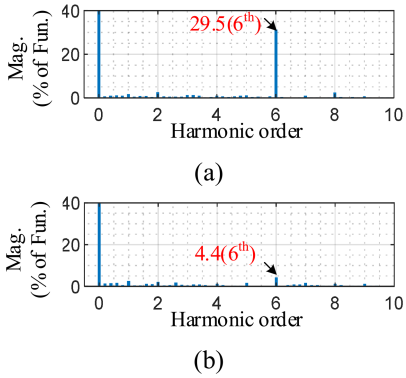

Fig. 14. FFT spectrum analysis of the q-axis current. (a)Without AIMC. (b) AIMC.

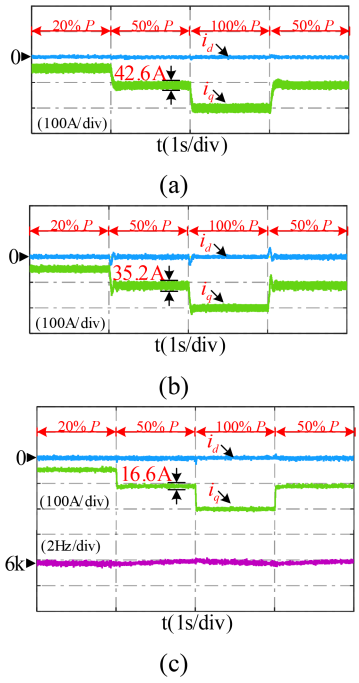

Fig. 15. Comparison of experiment results with load power change. (a) PI controller. (b) LADRC. (c) Proposed ANADRC.

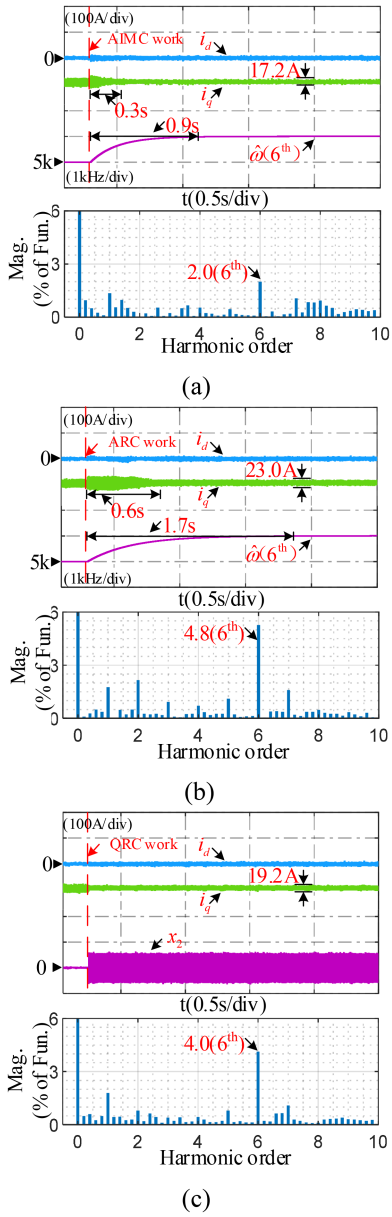

Fig. 16. Dynamic performance comparison experiment of adaptive methods under periodic disturbances. (a) Proposed AIMC. (b) ARC [29]. (c) QRC [25].

of the q-axis current error in AIMC is nearly six times the fundamental frequency and is unaffected by dc bus voltage variations.

Fig. 14 compares the fast Fourier transform (FFT) spectrum analysis of the q-axis current before and after applying AIMC. Without AIMC, the severe 5th and 7th harmonic components in the phase current manifest as a 6th harmonic in the q-axis current. After applying AIMC, the 6th harmonic content decreases from 29.5% to 4.4%. The experimental results validate the effectiveness of AIMC in suppressing current harmonics.

Fig. 15 presents the dq-axis current curves under different current controllers during load power changes. The results indicate that the amplitude of dq-axis current fluctuations is minimally affected by load variations. The PI controller and traditional LADRC controller exhibit significant ripple in the q-axis current. In particular, the LADRC, due to a large SEF, exacerbates dq-axis current coupling. In contrast, the proposed ANADRC controller, with the variable gain, virtually eliminates dq-axis current coupling during step load changes. The AIMC exhibits only minor frequency changes in q-axis current estimation under step load conditions, with frequency fluctuations not exceeding 0.5 Hz at full load, which can be considered negligible. Moreover, the effectiveness of AIMC in suppressing current harmonics is unaffected by nonperiodic load disturbances.

C. Dynamic Performance Experiment for Current Harmonic Suppression

Fig. 16 compares the experimental results of the proposed AIMC with the ARC and QRC in suppressing periodic disturbances [25], [29]. To highlight the suppression effect on periodic

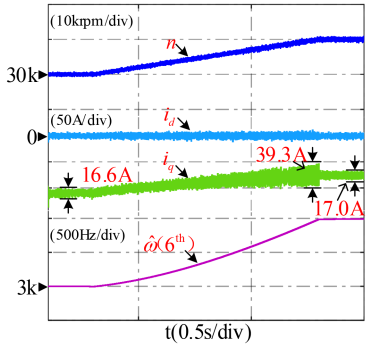

Fig. 17. Experiment on the dynamic performance of the current loop during the prime mover acceleration process.

disturbances, subsequent experiments use the PI controller with a higher content of 5th and 7th harmonics. The proposed AIMC can quickly track the frequency of the 6th harmonic in the q-axis current. At the initial operating point of the adaptive control, the estimated frequency does not match the actual frequency, leading to incorrect compensation voltage output by the AIMC and causing brief current fluctuations. This issue can be corrected by optimizing the AIMC intervention timing, which is determined by calculating the rate of change in the estimated frequency over two control cycles. Fig. 16(b) presents the experimental results of the recently proposed ARC for this research direction. It is evident that this resonant controller is designed for low-speed motors, resulting in slower tracking of disturbance frequencies. Consequently, it causes larger initial current fluctuations, and both the recovery to steady-state and the convergence time of the estimated frequency are slower compared to the proposed AIMC.

Fig. 16(c) shows the experimental results of the QRC, where the frequency can only be preset to 1000 Hz without disturbance identification capability. Since the preset frequency is close to the actual value, the q-axis current ripple reaches a steady-state value immediately upon QRC activation. As indicated by the QRC output x_2, the output remains constant. Due to fluctuations in system speed, the disturbance frequency also fluctuates, resulting in weaker suppression of the 5th and 7th harmonics by the QRC compared to the AIMC. The FFT spectrum analysis of the q-axis current shows that in steady-state, the proposed AIMC exhibits stronger suppression of the 6th harmonic compared to the ARC.

The literature [29] concludes that the ARC is effective in suppressing periodic disturbances only during steady-state conditions, and it is ineffective during dynamic processes. Fig. 17 presents the experimental results of the proposed AIMC during the prime mover acceleration process. The 5th and 7th harmonic frequencies of the phase current are influenced only by the motor speed, causing the 6th harmonic frequency of the q-axis current to increase during the prime mover acceleration. AIMC can estimate the disturbance frequency during dynamic processes. However, due to the inability to track frequency changes in real-time, the effectiveness of current harmonic suppression diminishes as the frequency error increases during acceleration.

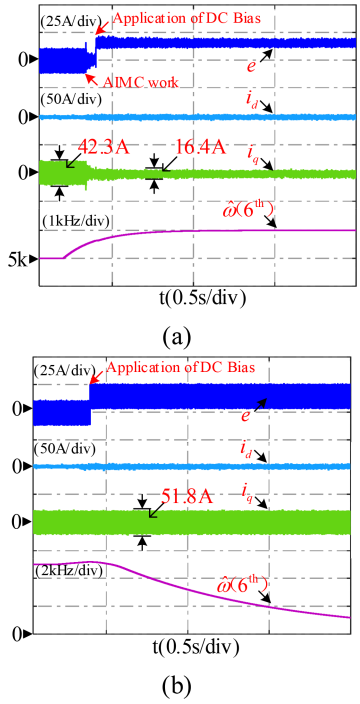

Fig. 18. Comparison of experimental results for dc bias under no-load conditions. (a) Proposed AIMC. (b) ARC [29].

Once the motor speed stabilizes, the harmonic suppression effect of the current rapidly returns to a steady-state level.

D. Experiment With DC Bias Noise

Fig. 18(a) presents the experimental results of the current loop with dc bias under the proposed AIMC controller. The AIMC incorporates the departure determination method described in the previous section, activating compensation when the estimated frequency closely aligns with the actual frequency. This approach avoids current fluctuations caused by mismatched frequency estimates. At $t = 0.4$ s, a 15 A dc bias is injected into the q-axis current, resulting in a brief disturbance in the estimated frequency before it stabilizes. Finally, the estimated frequency tracks the actual value, and the impact of the dc bias is mitigated by the x_3 loop of AIMC.

Fig. 18(b) shows the experimental results under the same conditions using an ARC. Without the injection of dc bias, the AFL can normally estimate the disturbance frequency. However, upon the introduction of the dc bias, the resonant controller's frequency estimation diverges. Due to significant frequency error, the compensation of resonant controller fails to engage, rendering it ineffective in suppressing periodic disturbances in the current loop. These experimental results validate the strong anti-interference capability of the proposed AIMC against dc bias.

E. Experiment of Parameter Robustness

Fig. 19 compares the experimental results of different controllers under motor parameter mismatch. During the controller

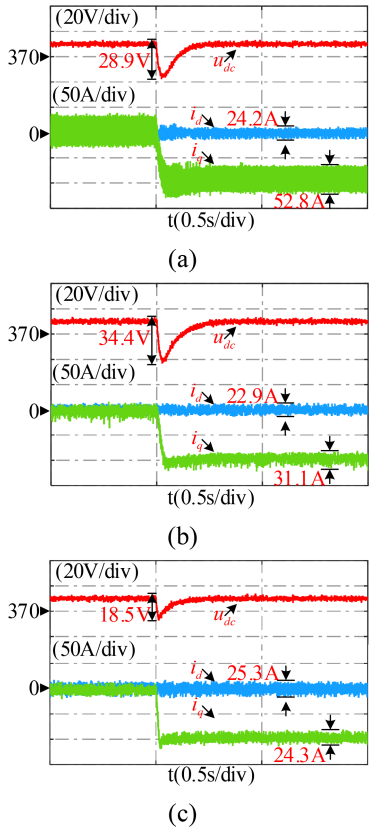

Fig. 19. Comparison experiment of different methods under L_s mismatch. (a) PI controller. (b) LNADRC. (c) ANADRC.

parameter tuning process, it is evident that the motor inductance affects the proportional gain k_{pi} of the PI controller and the gain coefficient b_0 of the ADRC. A motor inductance greater than the estimated value improves current quality [36]. Therefore, experiments in this section are conducted under conditions of relatively low inductance to emphasize degraded current ripple. By adjusting the relevant control parameters, the motor inductance is simulated as $0.5 * L_s$.

Compared to the results with nominal parameters in Section V-A, the PI and traditional ADRC controllers exhibit increased d/q-axis current ripple under inductance mismatch. The proposed control strategy shows the smallest increase in current ripple under similar parameter mismatches. Experimental results verify that the proposed ANADRC improves robustness to model parameter variations, although dependence on model parameters remains high. To ensure comprehensive system performance, a motor parameter identification method should be integrated with ADRC as an auxiliary component to adjust control parameters through online motor parameter identification. This integration will be pursued in future research to address these limitations.

VI. Conclusion

This article proposes a current control method based on adaptive ADRC disturbance suppression to address the current ripple issue in PMSG used in distributed generation system. The improved method integrates the advantages of both traditional LADRC and NADRC, having the best suppression performance against different forms of nonperiodic disturbances. Experimental results show that this method effectively enhances the disturbance rejection capability of the current loop and significantly improves current tracking performance. Compared to traditional control methods, this method demonstrates superior antidisturbance performance under uncertain periodic disturbances. However, the control effectiveness under motor parameter variations requires further optimization. Future research will integrate online parameter identification and adjustment strategies to improve the robustness of system parameters. The findings provide a reliable theoretical basis for the practical application of precise current control for onboard distributed generation system.

References

[1] A. Upadhyaya and C. Mahanta, "An overview of battery based electric vehicle technologies with emphasis on energy sources, their configuration topologies and management strategies," *IEEE Trans. Intell. Transp. Syst.*, vol. 25, no. 2, pp. 1087–1111, Feb. 2024.

[2] I. Aharon and A. Kuperman, "Topological overview of powertrains for battery-powered vehicles with range extenders," *IEEE Trans. Power Electron.*, vol. 26, no. 3, pp. 868–876, Mar. 2011.

[3] Z. Huang, J. Fang, X. Liu, and B. Han, "Loss calculation and thermal analysis of rotors supported by active magnetic bearings for high-speed permanent-magnet electrical machines," *IEEE Trans. Ind. Electron.*, vol. 63, no. 4, pp. 2027–2035, Apr. 2016.

[4] S. Wu, X. Sun, and W. Tong, "Optimization design of high-speed interior permanent magnet motor with high torque performance based on multiple surrogate models," *CES Trans. Elect. Mach. Syst.*, vol. 6, no. 3, pp. 235–241, 2022.

[5] Z. Lyu, L. Wu, and P. Song, "A novel harmonic current control method for torque ripple reduction of SPMSM considering DC-link voltage limit," *IEEE Trans. Power Electron.*, vol. 39, no. 2, pp. 2558–2568, Feb. 2024.

[6] C. Peng, J. Sun, X. Song, and J. Fang, "Frequency-varying current harmonics for active magnetic bearing via multiple resonant controllers," *IEEE Trans. Ind. Electron.*, vol. 64, no. 1, pp. 517–526, Jan. 2017.

[7] Z. Zhang and L. Xu, "Dead-time compensation of inverters considering snubber and parasitic capacitance," *IEEE Trans. Power Electron.*, vol. 29, no. 6, pp. 3179–3187, Jun. 2014.

[8] J. Han, "From PID to Active disturbance rejection control," *IEEE Trans. Ind. Electron.*, vol. 56, no. 3, pp. 900–906, Mar. 2009.

[9] L. Rosado, J. Samanes, E. Gubia, and J. Lopez, "Selective harmonic mitigation: Limitations of classical control strategies and benefits of model predictive control," *IEEE Trans. Ind. Appl.*, vol. 59, no. 5, pp. 6082–6094, Sep./Oct. 2023.

[10] J. Hong and R. Cao, "Adaptive selective harmonic elimination Model predictive control for three-level T-type inverter," *IEEE Access*, vol. 8, pp. 157983–157994, 2020.

[11] J. Perez, S. Cobreces, R. Grino, and F. J. R. Sanchez, "H∞ current controller for input admittance shaping of VSC-based grid applications," *IEEE Trans. Power Electron.*, vol. 32, no. 4, pp. 3180–3191, Apr. 2017.

[12] W. Chen, J. Yang, L. Guo, and S. Li, "Disturbance-observer-based control and related methods—An overview," *IEEE Trans. Ind. Electron.*, vol. 63, no. 2, pp. 1083–1095, Feb. 2016.

[13] X. Li, W. Tian, X. Gao, Q. Yang, and R. Kennel, "A generalized observer-based robust predictive current control strategy for PMSM drive system," *IEEE Trans. Ind. Electron.*, vol. 69, no. 2, pp. 1322–1332, Feb. 2022.

[14] L. Qu, W. Qiao, and L. Qu, "Active-disturbance-rejection-based sliding-mode current control for permanent-magnet synchronous motors," *IEEE Trans. Power Electron.*, vol. 36, no. 1, pp. 751–760, Jan. 2021.

[15] A. A. Godbole, J. P. Kolhe, and S. E. Talole, "Performance analysis of generalized extended State observer in tackling sinusoidal disturbances," *IEEE Trans. Control Syst. Technol.*, vol. 21, no. 6, pp. 2212–2223, Nov. 2013.

[16] S. Wodyk and G. Iwanski, "Active power filter control with vibrating coordinates transformation," *IEEE Trans. Power Del.*, vol. 38, no. 1, pp. 376–386, Feb. 2023.
[17] M. Liserre, R. Teodorescu, and F. Blaabjerg, "Multiple harmonics control for three-phase grid converter systems with the use of PI-RES current controller in a rotating frame," *IEEE Trans. Power Electron.*, vol. 21, no. 3, pp. 836–841, May 2006.
[18] V. M. Moreno, M. Liserre, A. Pigazo, and A. Dell'Aquila, "A comparative analysis of real-time algorithms for power signal decomposition in multiple synchronous reference frames," *IEEE Trans. Power Electron.*, vol. 22, no. 4, pp. 1280–1289, Jul. 2007.
[19] G. Liu, B. Chen, K. Wang, and X. Song, "Selective current harmonic suppression for high-speed PMSM based on high-precision harmonic detection method," *IEEE Trans. Ind. Inform.*, vol. 15, no. 6, pp. 3457–3468, Jun. 2019.
[20] Z. Chen, T. Shi, Z. Lin, Z. Wang, and X. Gu, "Analysis and control of current harmonic in IPMSM field-oriented control system," *IEEE Trans. Power Electron.*, vol. 37, no. 8, pp. 9571–9585, Aug. 2022.
[21] M. Tian, B. Wang, Y. Yu, Q. Dong, and D. Xu, "Discrete-time repetitive control-based ADRC for current loop disturbances suppression of PMSM drives," *IEEE Trans. Ind. Inform.*, vol. 18, no. 5, pp. 3138–3149, May 2022.
[22] Z. Wang, J. Zhao, L. Wang, M. Li, and Y. Hu, "Combined vector resonant and active disturbance rejection control for PMSLM current harmonic suppression," *IEEE Trans. Ind. Inform.*, vol. 16, no. 9, pp. 5691–5702, Sep. 2020.
[23] X. Yang, H. Hu, H. Hu, Y. Liu, and Z. He, "A quasi-resonant extended state observer-based predictive current control strategy for three-phase PWM rectifier," *IEEE Trans. Ind. Electron.*, vol. 69, no. 12, pp. 13910–13917, Dec. 2022.
[24] F. Yang et al., "Complex coefficient active disturbance rejection controller for current harmonics suppression of IPMSM drives," *IEEE Trans. Power Electron.*, vol. 37, no. 9, pp. 10443–10454, Sep. 2022.
[25] B. Wang, M. Tian, Y. Yu, Q. Dong, and D. Xu, "Enhanced ADRC with quasi-resonant control for PMSM speed regulation considering aperiodic and periodic disturbances," *IEEE Trans. Transp. Electrif.*, vol. 8, no. 3, pp. 3568–3577, Sep. 2022.
[26] X. Liu, Y. Deng, J. Wang, H. Li, and H. Cao, "Fixed-time generalized active disturbance rejection with quasi-resonant control for PMSM speed disturbances suppression," *IEEE Trans. Power Electron.*, vol. 39, no. 6, pp. 6903–6918, Jun. 2024.
[27] S. Zhu et al., "Robust speed control of electrical drives with reduced ripple using adaptive switching high-order extended state observer," *IEEE Trans. Power Electron.*, vol. 37, no. 2, pp. 2009–2020, Feb. 2022.
[28] R. Miklosovic, A. Radke, and Z. Gao, "Discrete implementation and generalization of the extended state observer," in *Proc. IEEE Amer. Control Conf.*, 2006, Paper no 6.
[29] M. Tian, B. Wang, Y. Yu, Q. Dong, and D. Xu, "Adaptive active disturbance rejection control for uncertain current ripples suppression of PMSM drives," *IEEE Trans. Ind. Electron. (1982)*, vol. 71, no. 3, pp. 2320–2331, Mar. 2024.
[30] M. Tian, B. Wang, Y. Yu, Q. Dong, and D. Xu, "Robust adaptive resonant controller for PMSM speed regulation considering uncertain periodic and aperiodic disturbances," *IEEE Trans. Ind. Electron. (1982)*, vol. 70, no. 4, pp. 3362–3372, Apr. 2023.
[31] C. Zhang et al., "An adaptive ADRC strategy with weight function for propeller speed control and experimental verification in wind tunnel," *IEEE Trans. Transp. Electrif.*, vol. 10, no. 1, pp. 670–681, Mar. 2024.
[32] C. Zhang, C. Zhang, L. Li, and H. Liu, "An enhanced nonlinear ADRC speed control method for electric propulsion system: Modeling, analysis, and validation," *IEEE Trans. Power Electron.*, vol. 38, no. 4, pp. 4520–4528, Apr. 2023.
[33] Y. Zuo, X. Zhu, L. Quan, C. Zhang, Y. Du, and Z. Xiang, "Active disturbance rejection controller for speed control of electrical drives using phase-locking loop observer," *IEEE Trans. Ind. Electron. (1982)*, vol. 66, no. 3, pp. 1748–1759, Mar. 2019.
[34] H. K. K. A. P. V. Kokotovic, *Singular Perturbation Methods in Control: Analysis and Design*. London, U.K.: Academic, 1986.
[35] Z. Hao et al., "Linear/nonlinear active disturbance rejection switching control for permanent magnet synchronous motors," *IEEE Trans. Power Electron.*, vol. 36, no. 8, pp. 9334–9347, Aug. 2021.
[36] M. Tian, T. Wang, Y. Yu, Q. Dong, B. Wang, and D. Xu, "Integrated observer-based terminal sliding-mode speed controller for PMSM drives considering multisource disturbances," *IEEE Trans. Power Electron.*, vol. 39, no. 7, pp. 7968–7979, Jul. 2024.